3-D segmentation algorithm of small lung nodules in spiral CT images

3-D Segmentation Algorithm of Small Lung Nodules in Spiral CT Images

Stefano Diciotti, *Member, IEEE*, Giulia Picozzi, Massimo Falchini, Mario Mascalchi, Natale Villari, and Guido Valli

***Abstract*—Computed tomography (CT) is the most sensitive imaging technique for detecting lung nodules, and is now being evaluated as a screening tool for lung cancer in several large samples studies all over the world. In this report, we describe a semiautomatic method for 3-D segmentation of lung nodules in CT images for subsequent volume assessment. The distinguishing features of our algorithm are the following. 1) The user interaction process. It allows the introduction of the knowledge of the expert in a simple and reproducible manner. 2) The adoption of the geodesic distance in a multithreshold image representation. It allows the definition of a fusion–segregation process based on both gray-level similarity and objects shape. The algorithm was validated on low-dose CT scans of small nodule phantoms (mean diameter 5.3–11 mm) and *in vivo* lung nodules (mean diameter 5–9.8 mm) detected in the Italung-CT screening program for lung cancer. A further test on small lung nodules of Lung Image Database Consortium (LIDC) first data set was also performed. We observed a RMS error less than 6.6% in phantoms, and the correct outlining of the nodule contour was obtained in 82/95 lung nodules of Italung-CT and in 10/12 lung nodules of LIDC first data set. The achieved results support the use of the proposed algorithm for volume measurements of lung nodules examined with low-dose CT scanning technique.**

***Index Terms*—Computer-aided diagnosis, computer vision, lung cancer, lung nodules segmentation, medical imaging, multiscale processing, spiral computed tomography (CT).**

I. Introduction

LUNG CANCER is the leading cause of cancer death both in Europe [1] and in the United States [2]. The five-year survival rate is about 15%, and it has not significantly increased over the last 20 years. The same survival rate for subjects who have localized cancer at diagnosis is about 49% [2]. These figures suggest that early diagnosis of lung cancer can improve the effectiveness of the treatment. In earlier stages, lung cancer most commonly manifests itself radiologically as a solitary noncalcified pulmonary nodule. Computed tomography (CT) is superior to chest radiography for detecting pulmonary nodules, and is now being evaluated as a screening tool in several large samples studies all over the world [3]–[7].

Manuscript received October 12, 2006; revised January 25, 2007 and March 27, 2007. This work was supported by the Italian Ministry of Education, University, and Research under Grant 2003068017.

S. Diciotti and G. Valli are with the Department of Electronics and Telecommunications, University of Florence, 50100 Florence, Italy (e-mail: diciotti@asp.det.unifi.it; guido.valli@alice.it).

G. Picozzi, M. Falchini, M. Mascalchi, and N. Villari are with the Department of Clinical Physiopathology, University of Florence, 50100 Florence, Italy (e-mail: giulia.picozzi@unifi.it; m.falchini@dfc.unifi.it; m.mascalchi@dfc.unifi.it; n.villari@dfc.unifi.it).

Digital Object Identifier 10.1109/TITB.2007.899504

CT scans repeated after short-term follow-up are usually employed to investigate nodule changes over time. In fact, nodule growth is the most important clue to possible malignancy of small solitary pulmonary nodules (i.e., having a mean diameter $\leq$10 mm) identified in CT screening trials for lung cancer [8], [9]. The current measurement method of nodule sizes, the digital caliper, is a completely manual tool and enables only the estimation of linear measurements. According to the Early Lung Cancer Action Project (ELCAP) protocol [10], nodule mean diameter is the average of the maximum diameter and the largest diameter perpendicular to the maximum diameter, both measured on the CT image in which the nodule shows the maximum cross-sectional area. Such linear measurements do not take into account the actual 3-D shape of the nodule and possible asymmetric pattern of growth. The estimate of nodule volume offers substantial advantages: 1) the volume characterizes the size of the structure considering the complete 3-D data, and thus, is the most appropriate parameter to evaluate size changes; 2) volume measurements have the potential to increase the sensitivity of CT in demonstrating lesion growth, since an increase of only 26% of diameter corresponds to a doubling of the volume for a spherical lung nodule; and 3) 3-D measurements show better intraoperator and interoperator reproducibility with respect to diameter estimations [11]–[13], due to the reduced operator dependence of the measuring process.

Lung nodule volume is usually determined after a segmentation procedure by using one of several methods: a simple voxel counting algorithm [14], the application of the divergence theorem [15], or methods that compensate for partial volume effects [14], [16]. In recent years, several algorithms have been investigated for lung nodule segmentation. Thresholding methods have been widely exploited. Several criteria, based on *in vitro* and *in vivo* studies, have been adopted to choose a proper threshold value. Fixed [14], [16]–[19] and variable thresholding methods have been described [14], [19], [20], and selection of the threshold as function of the image gradient has also been considered [19], [21]. Simple thresholding methods are suitable for discriminating well-circumscribed lung nodules from pulmonary parenchyma, while for lung nodules near other anatomical structures with similar gray levels, like vessels or pleura, other strategies must be applied to avoid the inclusion of such structures in the segmentation object. The analysis of the shape of pulmonary structures is usually performed to separate lung nodules from surrounding structures, since for instance, lung nodules are typically ellipsoidal objects, while vessels exhibit a preferential direction. Several 3-D shape parameters have been utilized including compactness or sphericity factors, and surface

curvature analysis [19], [21]–[23]. Approaches based on morphological algorithms were described by several authors [16], [17], [24]. Kostis *et al*. [17] adopted a morphological opening with a fixed-size structuring element to separate small nodules from the attached vasculature, and an iterative dilation procedure to reconstruct nodule borders. Kuhnigk *et al*. [16] described a method for processing both small and large nodules taking into account that a more pronounced fusion between large nodules and vessels is usually present. Aoyama *et al*. [25] applied a nodule segmentation algorithm for the determination of the likelihood measure of malignancy of lung lesions. The procedure uses a multiple thresholding method for the creation of a set of gray level contour lines, and a dynamic programming technique was used to obtain a nodule outline. Okada *et al*. [26] strategy was based on a fit of the lung nodule with an ellipsoid with a Gaussian profile. The nodule volume was then calculated on the fitted model. An active contour method was also proposed [27]. It is based on three novel energy components that take advantages of 3-D information, such as 3-D gradient, 3-D curvatures, and a mask term that reduces the possibility of contour growth over the pleural wall.

In this report, we describe a semiautomatic algorithm for 3-D lung nodule segmentation in spiral CT scans for subsequent volume evaluation. The computational strategy is based on two main processing modules: a focus of attention stage and a 3-D region growing algorithm. Two key features emerge by these stages. 1) Pulmonary structures included in the volume of interest are automatically detected by the focus of attention and are displayed to the operator for visual inspection. It is up to the operator to confirm each pulmonary structure signaled by the algorithm as a correct detection or to discard it. The knowledge of the expert is thus introduced into the algorithm through a controlled user interaction. 2) The 3-D segmentation algorithm adopts geodesic influence zones in a multithreshold image representation to allow the achievement of fusion–segregation criteria based on both gray-level similarity and objects shape.

The method was validated on both synthetic phantoms and small lung nodules identified in subjects scanned as a part of Italung-CT lung cancer screening program [7]. A further test on small lung nodules of Lung Image Database Consortium (LIDC) first data set [28] was also performed.

II. Methods

A. Lung Nodules Classes

In a 3-D CT examination, a lung nodule is a blob-like object lighter than the background, with a typical spheroidal/ellipsoidal shape. Lung nodules are embodied in a complex anatomical structure. In the lungs, several objects of various sizes are present, such as bronchi and blood vessels, and sometimes their proximity to lung nodules can hinder nodule detection and hamper nodule segmentation. According to location and connection with surrounding pulmonary structures, lung nodules can be classified into four main classes (see Fig. 1) [17].

1) Well-circumscribed nodules: without any connection with other pulmonary structures.

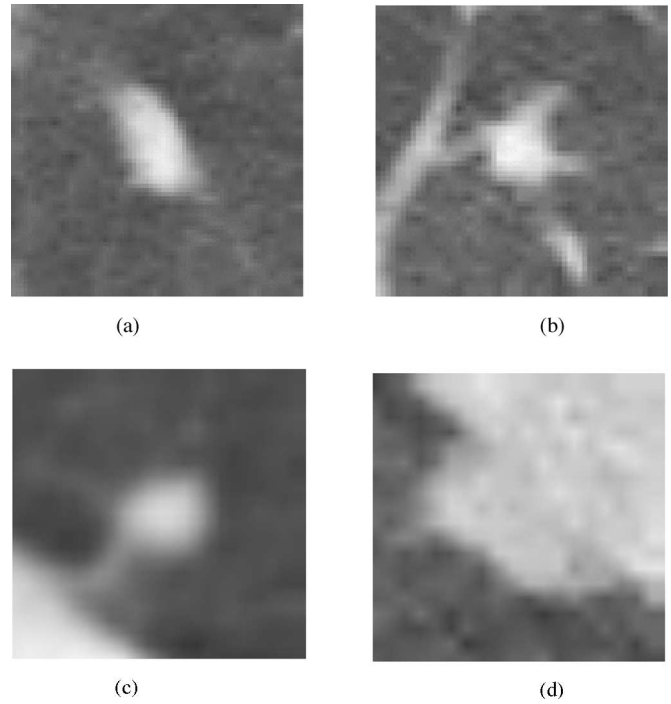

Fig. 1. Typical lung nodule for each class is shown. (a) Well-circumscribed nodule. (b) Juxta-vascular nodule. (c) Nodule with a pleural tail. (d) Juxta-pleural nodule.

2) Juxta-vascular nodule: there is a connection between the nodule and a vessel.
3) With pleural tail: there is a thin connection between the nodule and the pleural wall. The pleural tail is part of the nodule, and hence, has to be included in nodular segmentation. Therefore, differently from juxta-vascular nodules, the nonnodular structure must not be cut out to avoid underestimating the real nodule volume.
4) Juxta-pleural nodule: a high portion of the surface of the nodule is abutting the pleural wall. Juxta-vascular nodules are different from juxta-pleural ones due to a) the connection between the nodule and the nonnodular structure and b) the geometrical shape of the surrounding nonnodular structure.

In CT scans, vessels can be represented by blob-like structures with a local tubular shape. CT density of lung nodules and vessels are quite similar and their recognition requires prior knowledge of lung anatomy, including location, size, shape, and connections between the pulmonary structures.

In our method, we exploit the expert's knowledge by a controlled procedure as described in the following section. In this paper, nodules belonging to classes 3 and 4, which require a dedicated algorithm for pleural surface detection, were not considered.

B. Computational Strategy

The architecture of the algorithm is shown in Fig. 2. The operator selects the nodule of interest in the spiral CT images by using a custom computer user interface. As we are interested in

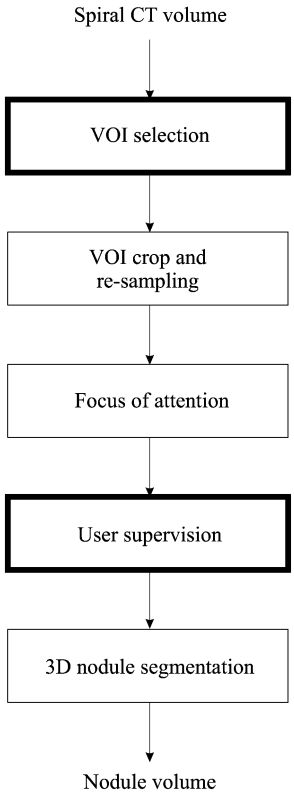

Fig. 2. Algorithm architecture for 3-D lung nodules segmentation. Bold rectangles indicate the stages in which user interaction is required.

assessing volumes of small nodules, a cubic volume of interest (VOI) of $25 \times 25 \times 25$ mm^3, centered in the voxel indicated by the operator, is extracted for further processing, and thus, we can assume that the nodule is completely included in the VOI. The VOI is supersampled with trilinear interpolation to obtain an isotropic voxel and to reduce partial volume effects [16], [17], [20]. The focus of attention stage identifies candidate markers corresponding to blob structures in the scale space. Each candidate marker is characterized by the location, scale, and contrast of the associated blob. The candidate marker, located within 2 mm from the center of the VOI and with the highest contrast, is automatically considered as a nodular marker.

All the candidate markers are shown to the observer for inspection. The observer has to confirm each candidate marker either as a nodular marker, a marker of a surrounding pulmonary structure, or as an object to discard. A 3-D region growing segmentation algorithm, described in detail in Section II-D, takes such markers into account in order to avoid a possible fusion between the nodule and different pulmonary structures. At the end of the segmentation stage, if the obtained segmentation is not successful, the procedure of marker supervision and the segmentation process can be repeated. The volume of the successful nodule segmentation is thus computed by using a reasonable and simple procedure, as the voxel counting method [14]. In any case, other methods for volume computation can also be employed.

To explain our method in the following, we shall refer to a 3-D computer simulation depicted in Fig. 3 including a synthetic spherical nodule and an elongated surrounding structure—both with a Gaussian profile and equal maximum value.

C. Focus of Attention

This stage detects and locates blob structures, identified as candidate markers for the lung nodules segmentation algorithm. A method for detecting blob patterns in a multiscale setting using Laplacian of Gaussian (LoG) kernels was proposed by Blostein and Ahuja [29]. They demonstrated that blob structures correspond to local maxima of LoG filtered images. LoG scale space was previously adopted in 2-D to detect lung nodules in chest radiograms with excellent results [30].

In a 3-D space [31], assuming $r = \sqrt{x^2 + y^2 + z^2}$, the LoG kernel can be written as

$$\begin{aligned}\mathrm{LoG}_\sigma(r) &= w(\sigma)\nabla^2 G_\sigma(r) \\ &= -\frac{w(\sigma)}{(2\pi)^{3/2}\sigma^5}\left(3 - \frac{r^2}{\sigma^2}\right)\exp\left(-\frac{r^2}{2\sigma^2}\right) \quad (1)\end{aligned}$$

where σ is the standard deviation (SD) of the Gaussian and $w(\sigma)$ is a normalization factor depending on σ. With the choice $-w(\sigma) = \sigma^2$, the volume of the central lobe of the LoG kernel is independent of σ and has a positive sign. In this way, it is possible to compare responses with a different σ. We shall refer to the width of the central lobe $h = 2\sqrt{3}\sigma$ as the scale parameter.

In accordance with the linear scale–space theory [32], let us consider the representation $L(x, y, z, h)$ of the volumetric image $f(x, y, z)$ as

$$L(x, y, z, h) = f(x, y, z) \otimes \mathrm{LoG}_h(x, y, z) \quad (2)$$

for the scales $h = h_{\min}, \ldots, h_{\max}$.

For each scale, local maxima of $L(x, y, z, h)$ are detected, and for each maxima, a coarse-to-fine tracking is applied and a scale–space signature [$L(x, y, z, h)$ versus h] is plotted [33]. It can be proven that the scale–space signature presents a marked peak for a certain scale h^*, suggesting the existence of a blob at that scale value h^*. We shall refer to this scale as the optimal scale, or the scale at which the normalized LoG response is maximal. The coordinates of the local maxima at the optimal scale are the estimated location of the blob structure.

It can be shown that the optimal scale h^* provides an estimate of blob size and that the value of LoG response at h^* estimates the blob contrast [32]. For the scale–space analysis, we considered a LoG family with $h = \{1, 2, \ldots, 10\}$ mm, and for scale–space tracking, a search region of $1 \times 1 \times 1$ voxels around each maxima.

Applying the focus of attention algorithm to the computer simulation of Fig. 3(a), six local maxima in the LoG scale space are detected. The candidate marker with the highest contrast within 2 mm from the VOI's center is automatically selected as a nodular marker. One of the other candidate markers identifies the center of the elongated structure while the remaining four can be related to border effects in LoG filtering. Each candidate marker and the automatically determined nodular marker are represented by circles in the slice corresponding to the z marker coordinate [Fig. 3(b)] with the estimated location as the center and the optimal scale as radius. Circle contour style and

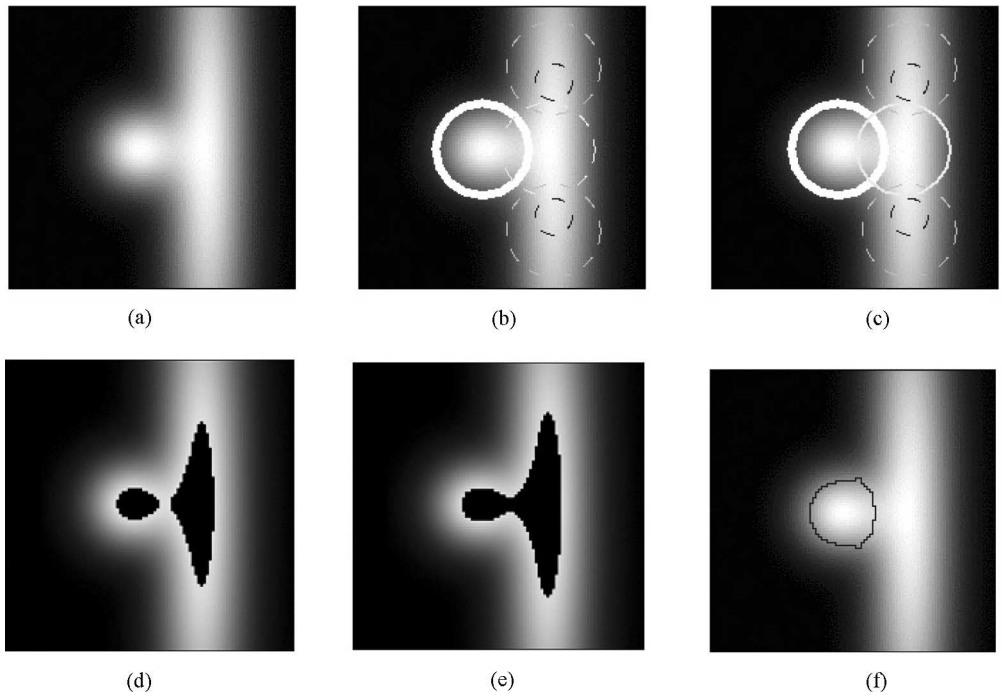

Fig. 3. Three-dimensional computer simulation composed of a spherical lung nodule on the left attached to an elongated structure on the right. The two objects have Gaussian profiles and the same maximum value. (a) Central slice of the 3-D image. (b) Results of the focus of attention stage represented by circles. The nodular marker is automatically selected and is represented by a solid thick line. (c) Marker of a non-nodule structure selected by the user and depicted with a solid thin line. Superimposed to the image (in black) the segmentation by thresholding with a value above the fusion value between the two structures in (d) and below the fusion value in (e). (f) Segmentation result of our algorithm.

thickness depend on the typology of the marker: dotted lines for candidate or ignored markers, solid thick lines for nodule markers, and solid thin lines for nonnodule markers. The LoG value at the optimal scale, that is the contrast of the considered structure, is represented by the circle's gray level, ranging from black (low values) to white (high values). With this graphic representation, black circles correspond to low contrast structures or image noise, while white circles correspond to more pronounced objects. Candidate markers, are thus, shown to the user for supervision. At this step, the user indicates, for each candidate marker, whether it is representative of the nodule, of the surrounding pulmonary structures, or of an object to discard. The candidate markers selected by the user become markers for the 3-D segmentation algorithm. In Fig. 3(c), a representation of the markers is shown after the user's supervision, in which one nonnodule marker was signaled and four candidate markers have been discarded by the user, and thus, ignored by the segmentation algorithm.

D. Three-Dimensional Segmentation Algorithm of Lung Nodules

We accomplish both the lung nodule and surrounding pulmonary structures segmentation by using a region growing approach. Region-based segmentation algorithms adopt fusion–segregation criteria based on gray-level similarity and proximity of the objects in the image. In our method, we join a gray-level representation with the geodesic distance concept, as described in the following (see Fig. 4).

Let $T_k(I) = \{p \in D_I \mid I(p) \geq k\}$ be the *threshold decomposition* of the 3-D image I, defined in the domain of the image voxels D_I. We consider the threshold values k lower or equal than the maximum Hounsfield (HU) value of the voxels selected as markers, both nodular and nonnodular, and greater than the HU value of the air (~ -1000 HU). The threshold value initially assumes the maximum possible value of the interval and decreases at each iteration by Δk, with a consequent growth of the number of voxels equal or greater than the selected threshold. The step decrement Δk must take a value not too high so that the growing of the $T_k(I)$ occurs with smoothness, but not too small to become too affected by image noise. A good compromise was experimentally reached fixing $\Delta k = 20$ HU. For each threshold value k, an opening morphological operation is applied to T_k, with a spherical structuring element of radius equal to 1 voxel, to separate regions connected by a reduced number of voxels, generally produced by image noise. Let $\overline{T_k}$ be the image resulting from the morphological processing. For a generic marker j, a region R_k^j composed of the voxel marker and of voxels of $\overline{T_k}$ that are six-neighborhood connected to the considered marker is produced. Let R_k^{nod} be the union of the regions connected with nodular markers and R_k^{sur} be the union of the regions connected to nonnodular markers. For a generic threshold value, the regions R_k^{nod} and R_k^{sur} could be disconnected or fused into one region. Generally, for high threshold values, the regions R_k^{nod} and R_k^{sur} are composed of a reduced number of voxels and are disconnected. By decreasing the threshold value k, the regions R_k^{nod} and R_k^{sur} growth and probability of fusion between them increases. In Fig. 3, the images $\overline{T_{k+\Delta k}}$ and $\overline{T_k}$

Input:
VOI image

1. Parameters initialization (k and Δk)
2. Compute VOI thresholding at level k
3. Perform a morphological opening
4. Determine the union of the regions connected to nodular markers (R_k^{nod}) and the union of the regions connected to non-nodular markers (R_k^{sur})
5. If R_k^{nod} and R_k^{sur} are not disconnected
   5.1 Assign 'new' voxels to the nearest connected region according to the geodesic distance
6. If a stop criterion is satisfied
   6.1 Go to step 10
7. Compute the mean magnitude of the image gradient on the nodule contour
8. Decrease k by Δk
9. Go to step 2
10. The optimal nodular segmentation is defined as the segmentation that has obtained the maximum mean magnitude gradient
11. Compute the nodule volume

Output:
nodule segmentation and volume

Fig. 4. Schema of our 3-D segmentation algorithm of lung nodules.

were shown superimposed on the VOI, for a threshold value above the fusion value between the two binary structures [at threshold value $k + \Delta k$ in (d)] and below the fusion value [at threshold value k in (e)]. In the first case, two separated regions are detected, one for a nodular marker and the other for the nonnodular structure, while in the second case, a unique connected region with both markers is identified. In the first case, R_k^{nod} constitutes the nodular segmentation for the current iteration, similarly to that described in [21]. In the second case, let $N = \overline{T_k} - \overline{T_{k+\Delta k}}$ be the set of "new" voxels appeared during the current growing step with respect to the previous one. At this point of the current iteration, the nodular region R_k^{nod} and the nonnodular region R_k^{sur} must be redefined in order to result disconnected.

For this purpose, we recall the concepts of geodesic distance and geodesic influence zones. According to Vincent *et al.* [34], the geodesic distance between two voxels x and y in set A is defined as the shortest length of the paths joining x and y and totally included in A [Fig. 5(a)]. Let us consider a set A and m connected regions $B_1, B_2, \ldots, B_m$ totally included in A [Fig. 5(b)]. The geodesic influence zone $iz_A(B_i)$ of a connected component B_i in A is the locus of the points of A whose geodesic distance to B_i is smaller than their geodesic distance to any other component of B. Keeping these definitions in mind, we assign each voxel of N according to the geodesic influence zones $iz_N(R_{k+\Delta k}^{\text{nod}})$ and $iz_N(R_{k+\Delta k}^{\text{sur}})$ defined in the $\overline{T_k}$ region with respect to the connected regions $R_{k+\Delta k}^{\text{nod}}$ and $R_{k+\Delta k}^{\text{sur}}$ (see Fig. 6). If the voxel belongs to $iz_N(R_{k+\Delta k}^{\text{nod}})$, it is assigned to R_k^{nod}, otherwise to R_k^{sur}. In other words, each voxel is associated to the nearest (according to the geodesic distance) connected region (nodular or nonnodular) obtained at the previous iteration, in which two disconnected regions were defined. In this way, a criterion of spatial proximity is adopted, when gray-level information only is not adequate to decide if a voxel belongs to a nodular or to a nonnodular region. The use of the geodesic distance allows one to keep the shape of the structures into account when calculating the distance between a voxel and a region, considering only the path inside a spatial region defined by voxels with gray level equal to or greater than a proper threshold. The selection criteria of the optimal nodular segmentation are based on the assumption that the nodule boundary is located where the mean magnitude of the image gradient calculated on the nodule contour is maximal [21] (see Fig. 7). For this purpose, the magnitude of the image gradient is initially determined, and for each growing step: 1) the mean magnitude of the gradient on the contour of the nodular segmentation is calculated and 2)

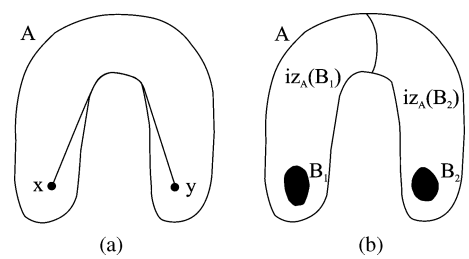

Fig. 5. (a) Example of a geodesic distance between voxels x and y in a region A is shown. (b) Geodesic influence zones are displayed for the regions B_1 and B_2 in A.

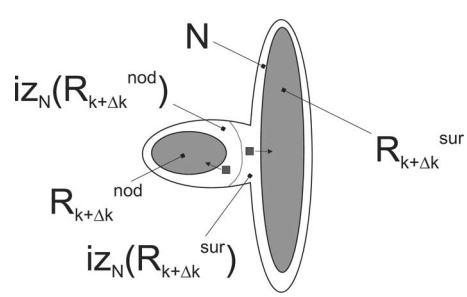

Fig. 6. Assignment of the voxels to the nodular or nonnodular regions according to the geodesic influence zones.

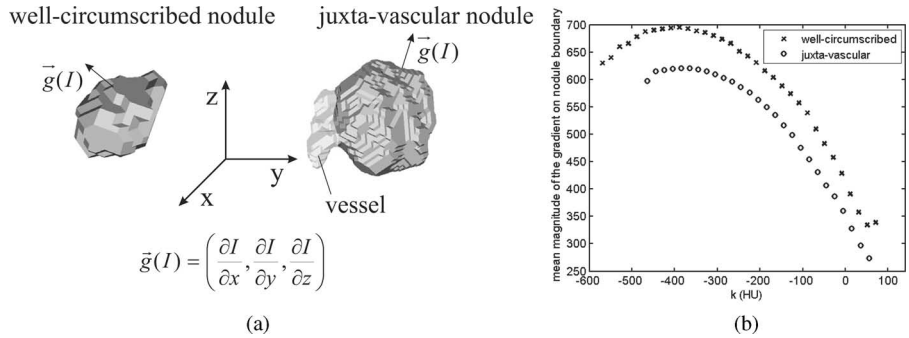

Fig. 7. (a) Two 3-D lung nodules segmentation are shown with the gradient vector displayed at the nodule boundary. (b) Plots of the mean magnitude of the gradient on the nodule boundary versus the threshold value are reported.

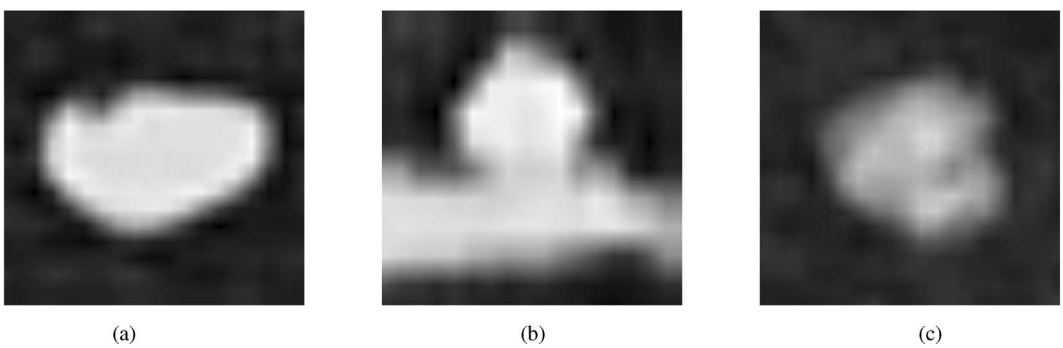

Fig. 8. CT slice of a phantom of type A, B, and C are shown in (a)–(c), respectively. The images are displayed with standard lung window settings (window level = −500 HU, window width = 1500 HU).

the optimal nodular segmentation is defined as the segmentation that has obtained the maximum mean magnitude gradient up to that iteration. The maximal gradient is searched for in the set of segmentations obtained at each iteration of the thresholding procedure. However, two practical rules can be adopted to terminate the procedure in advance, thus improving time performances without any change in segmentation results. The first rule is applied in the case in which a nodular region contains voxels belonging to the border of the VOI. That segmentation can be discarded because it is not in accordance with the hypothesis that the nodule has to be completely contained in the VOI, and the growing procedure can terminate. The second rule is related to the search of the maximal gradient. The plot of the gradient versus the threshold value for a high number of nodules was analyzed. It was observed that by decreasing the threshold value, if the maximal gradient on the contour of the nodule segmentation is not increased for six consecutive growing steps, that gradient value could be considered as the absolute maximum and the algorithm can be stopped.

III. Experimental Tests

The proposed procedures were implemented using C++ language in a Linux environment by using the Insight Segmentation and Registration Toolkit (ITK) [35] library for the image processing algorithms. The development and test platform was a PC equipped with an AMD Athlon XP 2400+ processor clocked at 2 GHz and with 512 MB of RAM memory. The processing time was, on the average, about 40 s for well-circumscribed nodules and about 120 s for juxta-vascular nodules. The focus of attention computation requires about 8 s, while the remaining time is needed for the 3-D segmentation algorithm.

Albeit very small nodules (<5 mm diameter) can be depicted in low-dose CT, screening trials focus on small nodules. Hence, we performed experimental tests on both small synthetic nodule phantoms and small lung nodules identified in a lung cancer screening program. An application of the proposed algorithm to lung nodules of LIDC first data set was also carried out.

A. Nodule Phantoms

We made three types of synthetic nodule phantoms (Fig. 8) to simulate *in vivo* lung nodules in different situations.

Type A: Forty silicone synthetic nodules (mean CT density ∼115 HU) with irregular shapes and known volume simulating well-circumscribed nodules [Fig. 8(a)]. The volume of the nodules was within the range 75.9–688.6 mm^3 (mean volume = 268.8 mm^3) corresponding to equivalent diameter (the diameter of a sphere with the same volume) within 5.3–11 mm (mean diameter = 8.0 mm). Each synthetic nodule was weighed on an analytical balance (Gibertini, 0.1-mg resolution) and the volume was computed dividing the weight by the density (0.98 g/cm^3) provided by the manufacturer of the material.

Type B: Ten silicone synthetic phantoms simulating nodules of known volume adjacent to a different structure, such as a blood vessel [Fig. 8(b)]. Ten type A phantoms were utilized to

simulate nodules. Each phantom was located in contact with an elongated structure made up of the same material adopted for type A phantoms.

Type C: Ten deformable well-circumscribed phantoms of silicone rubber mixed with polycarbonate microspheres [Fig. 8(c)]. The microspheres, commonly adopted in hobby modeling as fillers, contain air and decrease the CT density of the rubber at a mean value of ∼50 HU. The volume of these phantoms was not known. The phantoms were scanned before and after a deformation made by a hand manipulation. Due to the low values of pressure applied during the shape deformation, the phantoms, which are solids, cannot be compressed and preserve their volume unchanged.

All nodules were embedded in a marjoram (mean CT density ~ -865 HU) background to reproduce the texture of the lung parenchyma in the CT scans. Types A and B phantoms allowed the evaluation of the accuracy of the algorithm in volume measurements, while type C enabled the investigation of the behavior of the algorithm in the processing of nodules with the same volume but with a different shape.

B. Lung Nodules Data Sets

1) Italung-CT: We collected CT scans from subjects enrolled in the multicenter randomized clinical trial on lung cancer screening with low-dose thin-section CT, called *Italung-CT*, promoted and funded by the government of Tuscany Region (Italy) [7]. Ninety subjects showed 122 small nodules of indeterminate nature with mean diameter within 5 and 10 mm (6.4 ± 1.2 mm; range 5.0–9.8 mm). Ninety-eight nodules out of 122 belong to classes 1 and 2, while the remaining 24 nodules were of class 3 and 4, which were discarded. Three nodule examinations out of 98 were excluded due to technical artifacts. The proposed algorithm was then applied to the remaining 95 lung nodules.

2) LIDC First Data Set: As further independent test set, we adopted the data set collected by the LIDC [28]. The LIDC first data set is composed of CT examinations with 23 nodules from screening and diagnostic studies. All CT images have a matrix of 512×512 pixels and spacing between 0.605 and 0.742 mm. The cases are annotated by a panel of six expert radiologists [36].

We tested our algorithm on all solid nodules of LIDC first data set belonging to class 1 or 2 having mean diameter less than 10 mm, that is on four well-circumscribed and eight juxta-vascular nodules.

C. Nodule Phantoms and Italung-CT Images Acquisition

All nodule phantoms were scanned both with a single row of detector CT scanner (Somatom Plus 4; Siemens Medical System, Erlangen, Germany) and with four rows of detector CT scanner (Siemens Somatom Volume Zoom). All phantom images were acquired with low-dose thin-section CT acquisition protocols in use in the Italung-CT and with a high resolution CT (HRCT) standard dose protocol. Forty-eight subjects (having 28 well-circumscribed and 32 juxta-vascular nodules) undergoing Italung-CT were examined with the single row of detector and the remaining 42 (having eight well-circumscribed and 27 juxta-vascular nodules) with the four rows of detector scanner. *In vivo*, lung nodules were acquired by using only low-dose protocols, as part of the Italung-CT program. The low-dose protocols were denoted as low-dose single detector (LDSD) and low-dose multidetector (LDMD), respectively, for the single detector and the multidetector CT scanner. HRCT acquisition protocol was employed with the single detector CT scanner. The acquisition parameters of each CT protocol were detailed in Table I.

TABLE I
NODULE PHANTOMS AND ITALUNG-CT ACQUISITION PROTOCOLS

Parameter	Single row of detector scanner		4 rows of detector scanner
	HRCT	LDSD	LDMD
kV_p	140	140	140
mAs	159	43	40
field of view (mm)	340	340	340
collimation (mm)	1	3	1.25
pitch	1	2	7
reconstruction interval (mm)	1	1.5	1
reconstruction filter	AB91	AB91	B70f

D. Data Analysis

An expert radiologist examined the segmentation produced for each phantom and lung nodule on a computer monitor. To evaluate the accuracy of the algorithm in volume measurements, the RMS error was calculated in phantom tests of types A and B. Since different CT collimation width has been used, volume measurements were affected by different partial volume effects. To compensate for this phenomena, all phantom measurements were calibrated by using a linear function ($\mathrm{vol}_{\mathrm{true}} = a \times \mathrm{vol}_{\mathrm{meas}} + b$). For each CT acquisition protocol, a subset of 20 type A phantoms were randomly chosen to constitute a calibration set. The calibration parameters a and b were obtained with the least-square method, and the R^2 was calculated for each scan protocol. The linear calibration function was applied in all phantoms and Italung-CT lung nodule tests. No calibration data were available for LIDC first data set. For types A and B phantoms, absolute volume error was considered between the calibrated value and the true value [14]. For type A tests, only the phantoms not considered in the calibration process were taken into account for evaluation. The percentage of successful segmentations and the RMS errors were evaluated for each CT acquisition protocol.

To quantify the variability of volume measurements in phantoms of the same volume but of a different shape (type C phantoms), the Bland and Altman statistical method with 95% limits of agreement was applied in HRCT, LDSD, and LDMD cases. Preliminarily, for each CT protocol in type C phantom tests the correlation between the SD and the magnitude of volume measurements was evaluated using the Kendall τ test with a $p < 0.05$. In the case of a significant correlation, log-transformed data were employed [37], [38].

To assess the amount of interaction required to mark the structures proposed by the focus of attention, we recorded the number of nodular and nonnodular markers adopted for the

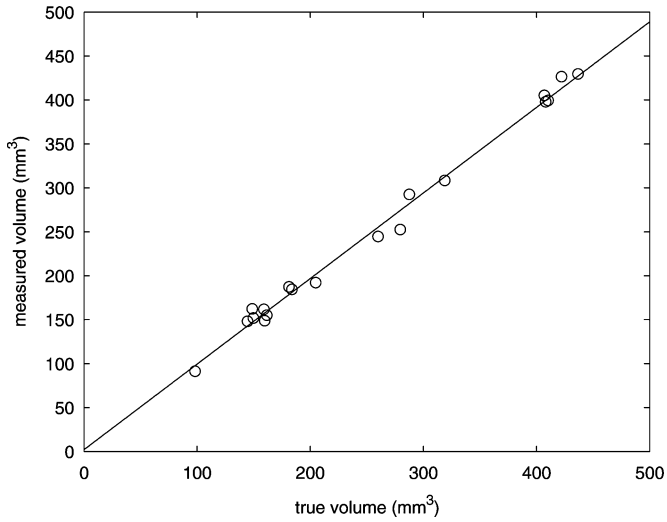

Fig. 9. Regression line for type A phantoms in LDSD scans.

segmentation of types A and B phantoms and lung nodules. The number of false positive segmentations (i.e., runs of the algorithm that do not carry out a correct segmentation but, with a different marker choice, become successful) of types A and B phantoms and lung nodules were also annotated.

IV. Results

A. Phantoms

According to radiologist's judgment for each CT protocol, all type A phantoms were successfully segmented. Phantoms of type B were correctly segmented in six out of ten cases in the LDSD cases and in ten out of ten cases both in LDMD and HRCT acquisitions. The algorithm showed an RMS error in 1.0%–6.6% for volume measurements of types A and B phantoms. The calibration coefficients, the R^2 values, and the RMS errors are reported in detail in Table II. In Fig. 9, the regression line for type A phantoms in LDSD acquisitions was shown. In Figs. 10 and 11, the volume percentage error versus equivalent diameter is shown for LDSD, LDMD, and HRCT protocols in type A tests. It should be noted that for any CT protocol, the volume percentage error decreases as the size of the nodule increases. All nodule phantoms and surrounding structures were automatically detected by the focus of attention stage. The number of the adopted nodular and nonnodular markers for phantoms of types A and B are reported in Table II. Mean and SD of false positive segmentations are also indicated in Table II.

Table III details the results of the Kendall τ test for volume measurements in type C phantoms. No significant correlation between SD and the magnitude of the volume measurements for any CT protocol was observed. The Bland and Altman 95% limits of agreement in type C phantom tests were -5.0% to 1.5% in HRCT acquisitions, -7.5% to 12.2% for LDSD scans, -7.4% to 5.6% in the LDMD case.

B. Lung Nodules

All nodules and vessels were automatically detected by the focus of attention stage. The number of nodular and nonnodular markers and the false positive segmentations are reported in Table IV.

1) Italung-CT: In 82 out of 95 nodules (86.3%), our method provided a successful segmentation. As detailed in Table IV, the percentage of successful segmentations were 97.2% and 79.7% for well-circumscribed and juxta-vascular nodules, respectively. In Figs. 12 and 13, the segmentation of two juxta-vascular nodules is shown Fig. 12 refers to a nodule examined with the LDSD CT protocol, while Fig. 13 refers to a nodule examined with the LDMD CT protocol. In each figure, the segmentation without any nonnodular marker and with a nonnodular marker was compared. Two slices of the 3-D VOI with superimposed the markers determined by the focus of attention stage are displayed in panels (a) and (b) for the segmentation without any nonnodular marker, and in panels (c) and (d) for the segmentation with a nonnodular marker. The marker in solid line and thick stroke was automatically selected by the algorithm and the marker in solid line and thin stroke was confirmed by the radiologist as nonnodular. Other markers were ignored. From panels (e) to (h) of both the figures, the segmentations of the corresponding slices showed from panels (a) to (d) are depicted. In particular, in panel (c) of Figs. 12 and 13, the nonnodular marker confirmed by the user allowed to avoid the fusion between the segmentation of the nodule and the vessel, clearly visible in panel (e) of each figure.

2) LIDC First Data Set: A correct segmentation was obtained in 10 out of 12 (83.3%) lung nodules. Exactly, all well-circumscribed nodules were successfully segmented together with six out of eight juxta-vascular nodules (see Table IV). The two nodules not correctly outlined were the #04 and #09. In Fig. 14, the segmentation of the nodule #03 is shown.

V. Discussion and Conclusion

We have proposed and tested a semiautomatic method for 3-D segmentation of lung nodules. Pulmonary structures in the neighborhood of the nodule, such as vessels, are automatically detected and confirmed by the operator to guide nodule segmentation. With only the automatic nodular marker selection, almost all well-circumscribed and some juxta-vascular nodules were correctly segmented. Juxta-vascular nodules require, on average, the confirmation of 0.9, 1.8, and 1.0 nonnodular markers for Italung-CT LDSD, Italung-CT LDMD category, and LIDC first data set, respectively.

A region growing algorithm keeps such markers into account by using geodesic distance zones in a multithreshold image representation. We believe that the adoption of the geodesic distance is a reasonable choice since voxels were assigned to the nearest region according to the shapes of the structures. On average, the false positive segmentations were at maximum 0.9 in the Italung-CT LDMD category for juxta-vascular nodules. Due to the geodesic approach applied after the confirmation of nonnodular markers, computational time is larger, but still limited,

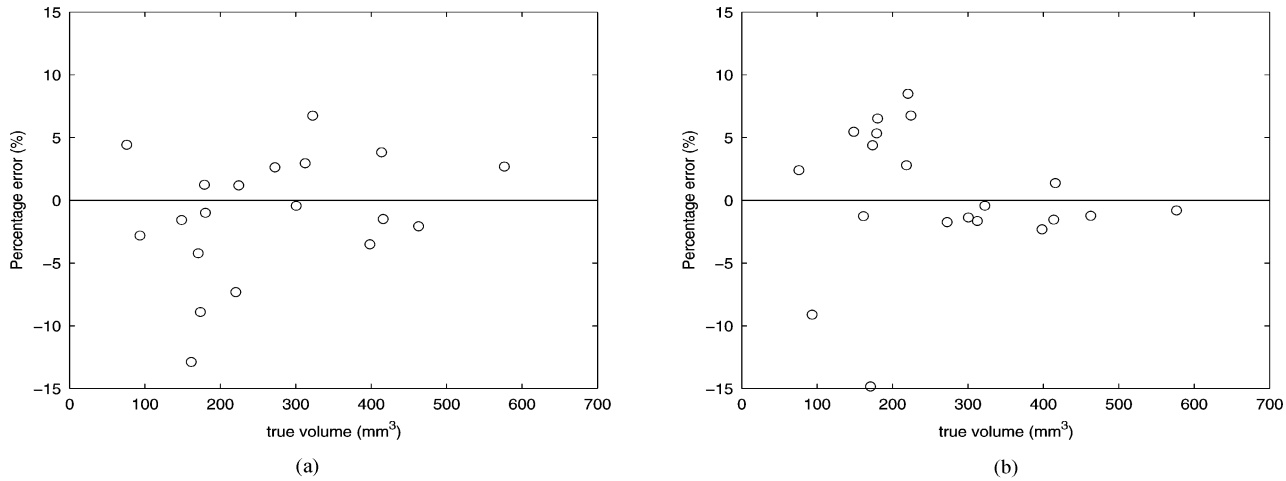

Fig. 10. Volume percentage error versus true volume for type A phantoms. (a) LDSD acquisitions. (b) LDMD acquisitions.

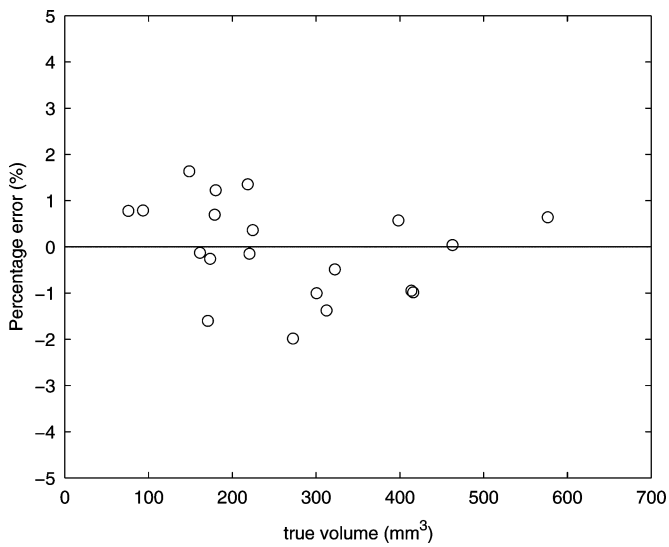

Fig. 11. Volume percentage error versus true volume for type A phantoms in HRCT acquisitions.

TABLE II
CALIBRATION COEFFICIENTS, R^2, AND RMS ERRORS FOR EACH CT PROTOCOL

	Phantom Type	HRCT	LDSD	LDMD
a	Any	0.9892	1.0274	0.9076
b	Any	-5.9149	-2.2363	1.0715
R^2	Any	0.9992	0.9961	0.9955
Number of nodular markers	Type A	1.0	1.0	1.0
	Type B	1.0	1.2±0.4	1.2±0.4
Number of non-nodular markers	Type A	0.0	0.0	0.0
	Type B	0.6 ± 1.3	2.2±1.9	0.9±0.7
false positive runs of the algorithm	Type A	0.0	0.0	0.0
	Type B	0.2±0.6	0.5±0.8	0.2±0.4
RMS error	Type A	1.0%	5.9%	5.4%
	Type B	5.8%	6.1%	6.6%

The number of the adopted nodular and nonnodular markers are also reported (mean and SD).

TABLE III
KENDALL τ CORRELATION COEFFICIENTS BETWEEN SD AND MAGNITUDE OF THE VOLUME MEASUREMENTS

CT Protocol	Kendall τ	p
HRCT	-0.24	0.33
LDSD	0.42	0.09
LDMD	-0.16	0.53

Relevant p values are also indicated.

for juxta-vascular nodules as compared to well-circumscribed nodules.

Since an user interaction is required, the effect of this manual intervention should be verified on the performance of the algorithm. For this reason, in another study, described in [39], both intraoperator and interoperator reproducibility of volume measurements were assessed on low-dose thin-section CT scans.

It is well known that volume measurements are heavily affected by CT image quality. As reported by Ko *et al.* [14], the best results are obtained with standard dose and sharp reconstruction kernel protocols. Moreover, collimation width plays an important role since it has a relevant influence on partial volume effects. Some previous studies on nodule phantoms were performed by other researchers. Yankelevitz *et al.* [40] obtained an RMS error of 3% on phantoms with size $\geq$3 mm examined with a standard dose and small field of view (FOV). Ko *et al.* [14] applied several algorithms for nodule segmentation based on fixed and variable thresholding. Partial volume methods were also proposed. The authors reported high errors (1.2–10.0 mm^3 for phantoms of size 8–60 mm^3) as compared to other studies, probably for the employment of large FOV and a realistic lung background. Recently, Kuhnigk *et al.* [16] reported a median error of -3.1% on juxta-vascular phantoms in standard and low-dose CT scans.

Ideally, a comparison between segmentation algorithms on lung nodules should be performed on a large public data set with a defined ground truth [16]. In the future, important resources still under construction, like the LIDC data set, will probably become a reference standard, but nowadays such archives are at an initial stage. As a matter of fact, most studies were performed on systems developed with private databases and, since segmentation performance is heavily affected by CT protocols and nodule characteristics, the comparison between different research groups remains, currently, quite limited.

TABLE IV
RESULTS OBTAINED FOR LUNG NODULES IDENTIFIED IN THE ITALUNG-CT AND FOR LUNG NODULES OF LIDC FIRST DATA SET

		Italung-CT		LIDC	
	CT Protocol	Well-circumscribed	Juxta-vascular	Well-circumscribed	Juxta-vascular
Number of nodular markers	LDSD	1.4 ± 1.7	1.0	1.0	1.0
	LDMD	1.0	1.4±0.4		
Number of non-nodular markers	LDSD	0.1±0.7	0.9±0.9	0.0	1.0±2.0
	LDMD	0.1±0.4	1.8±1.9		
false positive runs of the algorithm	LDSD	0.2±0.7	0.2±0.6	0.0	0.2±0.4
	LDMD	0.1±0.3	0.9±1.0		
Successful segmentations/ number of nodules	LDSD	27/28	29/32		
	LDMD	8/8	18/27		
	Overall	35/36 (97.2%)	47/59 (79.7%)	4/4 (100%)	6/8 (75%)

Overall successful segmentations were revealed in 82/95 (86.3%) nodules of Italung-CT and in 10/12 (83.3%) nodules of LIDC. The number of the adopted nodular and nonodular markers are also reported (mean and SD).

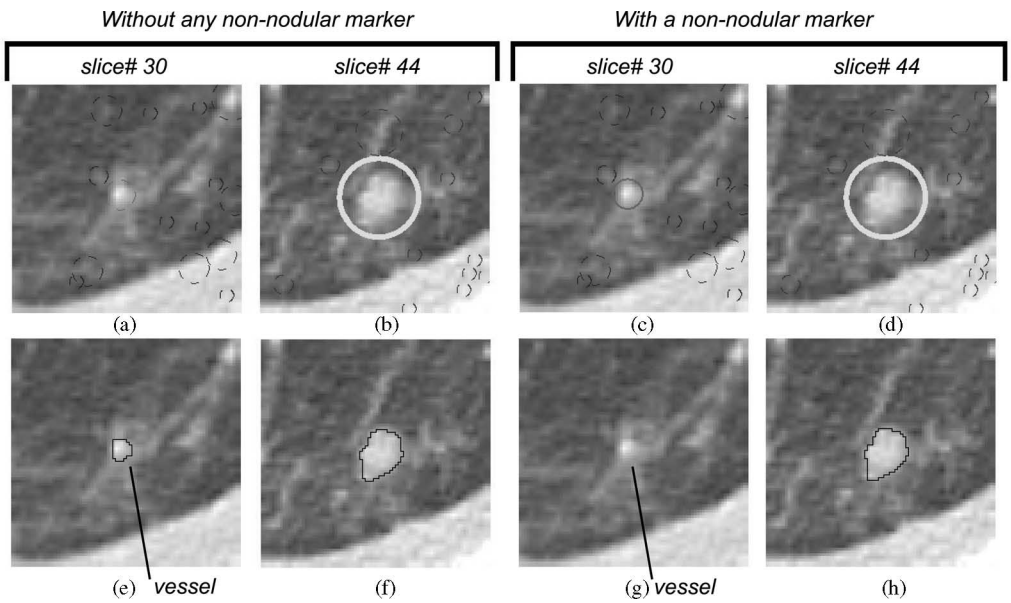

Fig. 12. Segmentation without and with the confirmation of a nonnodular marker of a juxta-vascular lung nodule of Italung-CT trial acquired with the LDSD CT protocol: two slices of the 3-D VOI with superimposed the markers are displayed in panels (a) and (b) for the segmentation without any nonnodular markers, and in panels (c) and (d) for the segmentation with a nonnodular marker; on the bottom [panels from (e) to (h)], the corresponding segmentations are displayed.

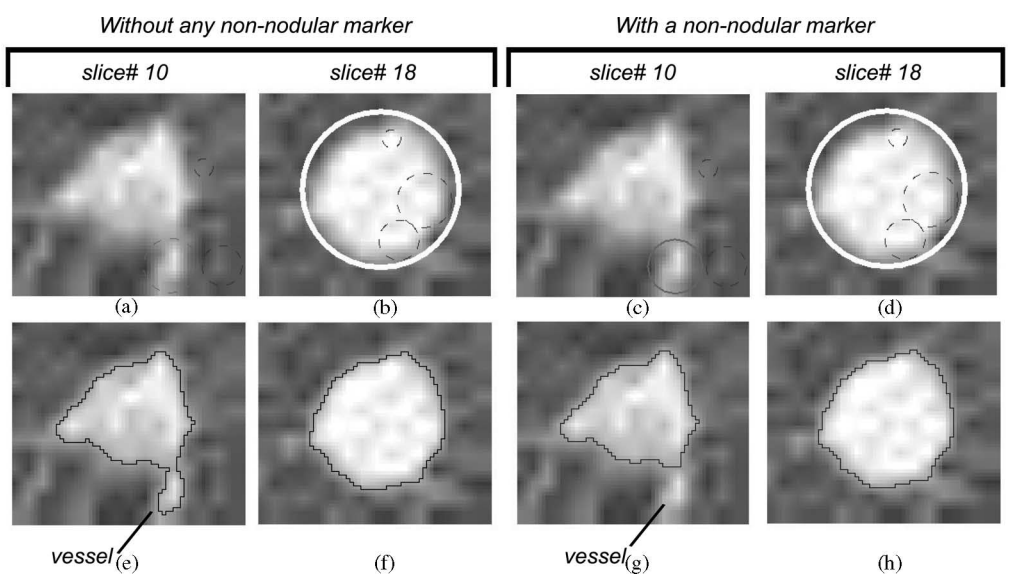

Fig. 13. Segmentation without and with the confirmation of a nonnodular marker of a juxta-vascular lung nodule of Italung-CT trial acquired with the LDMD CT protocol. See caption of Fig. 12 for panels explanation.

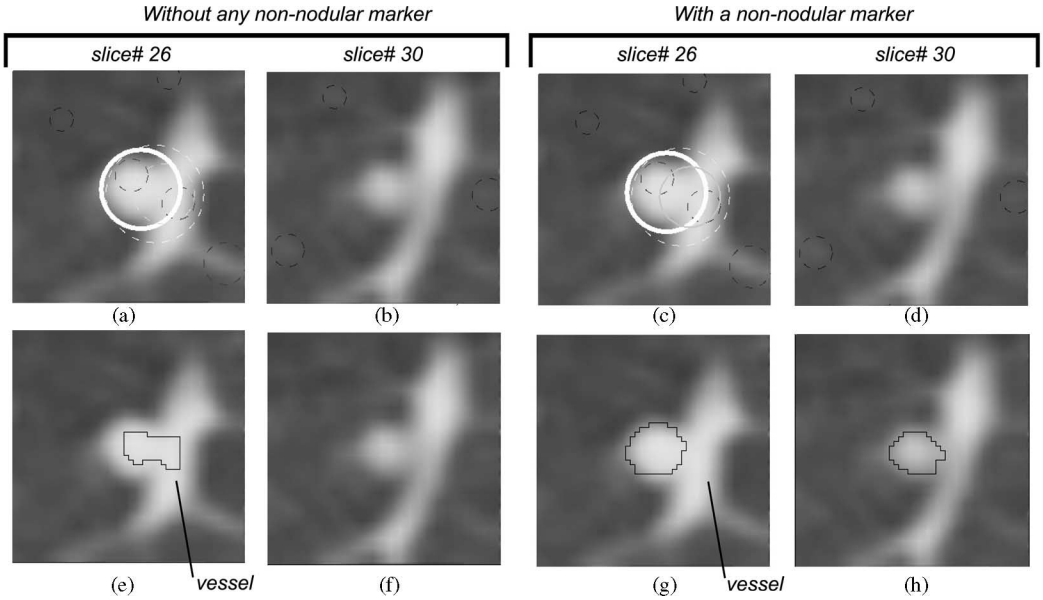

Fig. 14. Segmentation without and with the confirmation of a nonnodular marker of nodule #03 of LIDC first data set. See caption of Fig. 12 for panels explanation.

Kostis *et al.* [17] reported 80% of successful segmentations on a data set of 21 juxta-vascular nodules examined with standard dose acquisitions. With a free manual correction of the kernel size of a morphological operation, such a percentage increased to 95%. Kuhnigk *et al.* [16] achieved a high percentage of correct segmentation (91.4%) on a large data set of low-dose scans including small and large nodules. Lastly, Okada *et al.* [26] indicated about 81% of successful segmentations on two data sets including juxta-pleural and ground-glass opacities, all examined with HRCT.

In this paper, both a standard dose HRCT protocol (which ensures better image quality) and low-dose CT protocols, as used in lung cancer screening programs, were employed for *in vitro* validation. To study phantoms in similar conditions to those employed with *in vivo* lung nodules, we paid attention to the realistic model of synthetic phantoms and also on the use of a large FOV during image acquisitions. Nodule phantoms with irregular shape were made, both well circumscribed and in proximity to other structures. As regarding CT image density and texture, they were embodied in a material that simulates the lung parenchyma. All these factors are likely to affect the segmentation performances, and therefore, the volume estimation [14]. Moreover, we used large FOV, similar to that used in patient examinations, with the drawback of a reduced image quality. As a fact, CT images acquired with a large FOV show a worse in-plane spatial resolution and increased partial volume effects compared to those generated with a targeted (small) FOV [17], [40]. Hence, the use of a targeted FOV can produce more accurate volume estimations [14], but it is not recommended in current protocols for lung cancer screening [10].

For type A phantoms, in HRCT images, the RMS error was lower than in low-dose protocols due to both higher SNR and reduced partial volume effects. However, with LDSD and LDMD protocols, good performances were obtained since the RMS error was lower than 6%. In type B cases, the segmentation approach, based on the geodesic influence zones, permitted the detachment of nodules from surrounding pulmonary structures: the segmentations were all successful except in four phantoms in LDSD scans. With LDSD protocol, partial volume effects were more pronounced compared to LDMD and HRCT protocols because of the wider collimation width; therefore, a segmentation failure can more likely occur in the case of a nodule near other surrounding structures. It should be pointed out that a few studies have addressed the role of low-dose technique with respect to the accuracy (and reproducibility) of the nodule volume measurements [14], [16], [41], [42]. Like other researchers [14], we observed that volume measurements were significantly influenced by the scan dose, at least in *in vitro* studies in which a gold standard is available. Type C phantoms enabled us to explore the influence of the shape of the nodule in volumetric analysis. Bland and Altman's analysis revealed that volume measurements performed in phantoms examined with HRCT have reduced variability compared to that employed on low-dose scans. For example, if a nodule measurement of 300 mm^3 was performed, by varying only the shape of the nodule we should obtain, in another measurement process with a confidence level of 95%, a measurement between 277.8 and 316.8 mm^3.

In regard to lung nodules identified in the Italung-CT, we observed successful segmentations in 97.2% of well-circumscribed nodules and in 79.7% of juxta-vascular nodules. Overall, correct segmentations were obtained in 86.3% on the entire data set. No statistical comparison among the segmentation performances of nodules examined with different CT scanners was attempted. It will be performed as soon as results from extended samples are available. A further test on the LIDC first data set revealed a 83.3% of correct

segmentations (100% for well-circumscribed nodules and 75% for juxta-vascular nodules).

In conclusion, the results reached by the proposed method on phantoms and on *in vivo* nodules support the validity of the algorithm to analyze well-circumscribed and juxta-vascular nodules identified in a screening trial with low-dose thin-section CT.

ACKNOWLEDGMENT

The authors would like to thank the anonymous reviewers for their helpful comments about the preliminary version of this manuscript.

REFERENCES

[1] International Agency for Research on Cancer. (2005). [Online]. Available: http://www-dep.iarc.fr.

[2] American Cancer Society. (2005). Cancer fact and figures [Online]. Available: http://www.cancer.org/downloads/STT/CAFF2005f4 PWSecured.pdf.

[3] S. Diederich, M. Thomas, M. Semik, H. Lenzen, N. Roos, A. Weber, W. Heindel, and D. Wormanns, "Screening for early lung cancer with low-dose spiral computed tomography: Results of annual follow-up examinations in asymptomatic smokers," *Eur. Radiol.*, vol. 14, no. 4, pp. 691–702, Apr. 2004.

[4] S. Sone, L. Li, Z. G. Yang, T. Honda, Y. Maruyama, S. Takashima, M. Hasegawa, S. Kawakami, K. Kubo, M. Haniuda, and T. Yamanda, "Results of three-year mass screening programme for lung cancer using mobile low-dose spiral computed tomography scanner," *Brit. J. Cancer*, vol. 84, pp. 25–32, 2001.

[5] C. I. Henschke, D. F. Yankelevitz, J. P. Smith, O. M. Miettinen, ELCAP Group, "Screening for lung cancer: The early lung cancer action approach," *Lung Cancer*, vol. 35, pp. 143–148, 2002.

[6] S. J. Swensen, J. R. Jett, J. A. Sloan, D. E. Midthun, T. E. Hartman, A. M. Sykes, G. L. Aughenbaugh, F. E. Zink, S. L. Hillman, G. R. Noetzel, R. S. Marks, A. C. Clayton, and P. C. Pairolero, "Screening for lung cancer with low-dose spiral computed tomography," *Amer. J. Respir. Crit. Care Med.*, vol. 165, pp. 508–513, 2002.

[7] G. Picozzi, E. Paci, A. L. Pegna, M. Bartolucci, G. Roselli, A. D. Francisci, S. Gabbrielli, A. Masi, F. Perri, M. L. Rottoli, F. Carozzi, N. Villari, and M. Mascalchi, "Screening of lung cancer with low dose spiral CT. Results of a three year pilot study and design of the randomized clinical trial "Italung-CT"," *La Radiol. Med.*, vol. 109, pp. 17–26, Jan./Feb. 2005.

[8] D. M. Libby, J. P. Smith, N. K. Altorki, M. W. Pasmantier, D. Yankelevitz, and C. I. Henschke, "Managing the small pulmonary nodule discovered by CT," *Chest*, vol. 125, pp. 1522–1529, 2004.

[9] D. Yankelevitz, R. Gupta, B. Zhao, and C. Henschke, "Small pulmonary nodules: Evaluation with repeat CT-preliminary experience," *Radiology*, vol. 212, pp. 561–566, 1999.

[10] C. Henschke. (2006, Feb.) International Early Lung Cancer Action Program: Protocol [Online]. http://www.ielcap.org/ielcap.pdf, accessed May 31, 2006.

[11] M. Revel, C. Lefort, A. Bissery, M. Bienvenu, L. Aycard, G. Chatellier, and G. Frija, "Pulmonary nodules: Preliminary experience with three-dimensional evaluation," *Radiology*, vol. 231, pp. 459–466, 2004.

[12] L. Goodman, M. Gulsun, L. Washington, P. Nagy, and K. Piacsek, "Inherent variability of CT lung nodule measurements in vivo using semi-automated volumetric measuements," *Amer. J. Roentgenol.*, vol. 186, pp. 989–994, 2006.

[13] K. Marten, F. Auer, S. Schmidt, G. Kohl, E. Rummeny, and K. Engelke, "Inadequacy of manual measurements compared to automated CT volumetry in assessment of treatment response of pulmonary metastases using RECIST criteria," *Eur. Radiol.*, vol. 16, pp. 781–790, 2006.

[14] J. P. Ko, H. Rusinek, E. L. Jacobs, J. S. Babb, M. Betke, G. McGuinness, and D. P. Naidich, "Small pulmonary nodules: Volume measurement at chest CT-phantom study," *Radiology*, vol. 228, no. 8, pp. 864–780, 2003.

[15] A. M. Alyassin, J. L. Lancaster, J. H. Downs, III, and P. T. Fox, "Evaluation of the new algorithms for the interactive measurement of surface area and volume," *Med. Phys.*, vol. 21, no. 6, pp. 741–752, Jun. 1994.

[16] J. Kuhnigk, V. Dicken, L. Bornemann, A. Bakai, D. Wormanns, S. Krass, and H. Peitgen, "Morphological segmentation and partial volume analysis for volumetry of solid pulmonary lesions in thoracic CT scans," *IEEE Trans. Med. Imag.*, vol. 25, no. 4, pp. 417–434, Apr. 2006.

[17] W. Kostis, A. Reeves, D. Yankelevitz, and C. Henschke, "Three-dimensional segmentation and growth-rate estimation of small pulmonary nodules in helical CT images," *IEEE Trans. Med. Imag.*, vol. 22, no. 10, pp. 1259–1274, Oct. 2003.

[18] J. Goo, T. Tongdee, R. Tongdee, K. Yeo, C. Hildebolt, and K. Bae, "Volumetric measurement of synthetic lung nodules with multi-detector row CT: Effect of various image reconstruction parameters and segmentation thresholds on measurement accuracy," *Radiology*, vol. 235, pp. 850–856, 2005.

[19] W. Mullally, M. Betke, and J. Wang, "Segmentation of nodules on chest computed tomography for growth assessment," *Med. Phys.*, vol. 31, no. 4, pp. 839–848, 2004.

[20] A. Reeves, A. Chan, D. Yankelevitz, C. Henschke, B. Kressler, and W. Kostis, "On measuring the change in size of pulmonary nodules," *IEEE Trans. Med. Imag.*, vol. 25, no. 4, pp. 435–450, Apr. 2006.

[21] B. Zhao, A. Reeves, D. Yankelevitz, and C. Henschke, "Three-dimensional multicriterion automatic segmentation of pulmonary nodules of helical computed tomography images," *Opt. Eng.*, vol. 38, no. 8, pp. 1340–1347, 1999.

[22] Y. Kawata, N. Niki, H. Oshmatsu, K. Eguchi, and N. Moriyama, "Shape analysis of pulmonary nodules based on thin section CT images," in *Proc. SPIE*, 1997, vol. 3034, pp. 964–974.

[23] J. Kostis, A. Reeves, D. Yankelevitz, and C. Henschke, "Three-dimensional curvature analysis of small pulmonary nodules in helical CT scans," in *Proc. RSNA Scientific Program 2000, Suppl. Radiol.*, Nov., vol. 217P, p. 549.

[24] C. Fetita, F. Preteaux, C. Beigelman-Aubry, and P. Grenier, "3D automatic lung nodule segmentation in HRCT," in *Proc. MICCAI*, (Series Lecture Notes in Computer Science 2878) R. E. Ellis and T. M. Peters, Eds. Berlin, Germany: Springer-Verlag, pp. 626–634, 2003.

[25] M. Aojama, Q. Li, S. Katsuragawa, F. Li, S. Sone, and K. Doi, "Computerized scheme for determination of the likelihood measure of malignancy for pulmonary nodules on low-dose CT images," *Med. Phys.*, vol. 30, no. 3, pp. 387–394, Mar. 2003.

[26] K. Okada, D. Comaniciue, and A. Krishnan, "Robust anisotropic gaussian fitting for volumetric characterization of pulmonary nodules in multi-slice CT," *IEEE Trans. Med. Imag.*, vol. 24, no. 3, pp. 409–423, Mar. 2005.

[27] T. Way, L. Hadjilski, B. Sahiner, H. Chan, P. Cascade, E. Kazerooni, N. Bogot, and C. Zhou, "Computer-aided diagnosis of pulmonary nodules on CT scans: Segmentation and classification using 3D active contours," *Med. Phys.*, vol. 33, no. 7, pp. 2323–2337, 2006.

[28] K. W. Clark, D. S. Gierada, S. M. Moore, D. R. Maffitt, P. Koppel, S. R. Phillips, and F. Prior, "Creation of a CT image library for the lung screening study of the national lung screening trial," *J. Digit Imag.*, vol. 20, no. 1, pp. 23–31, Mar. 2007.

[29] D. Blostein and N. Ahuja, "Shape from texture: Integrating texture-element extraction and surface estimation," *IEEE Trans. Pattern Anal. Mach. Intell.*, vol. 11, no. 12, pp. 1233–1251, Dec. 1989.

[30] G. Coppini, S. Diciotti, M. Falchini, N. Villari, and G. Valli, "Neural networks for computer aided diagnosis: Detection of lung nodules in chest radiograms," *IEEE Trans. Inf. Technol. Biomed.*, vol. 7, no. 4, pp. 344–357, Dec. 2003.

[31] S. Diciotti, L. Petrolo, M. Falchini, G. Picozzi, M. Mascalchi, N. Villari, and G. Valli, "Multi-scale neural network system for lung nodules detection in spiral CT images: Preliminary results," presented at the Mediterr. Conf. Med. Biol. Eng., IFMBE, Ischia, Italy, 2004.

[32] T. Lindeberg, *Scale-Space Theory in Computer Vision*. Dordrecht, The Netherlands: Kluwer, 1994.

[33] T. Netsch and H. Peitgen, "Scale-space signatures for the detection of clustered microcalcifications in digital mammograms," *IEEE Trans. Med. Imag.*, vol. 18, no. 9, pp. 774–786, Sep. 1999.

[34] L. Vincent and P. Soille, "Watershed in digital spaces: An efficient algorithm based on immersion simulations," *IEEE Trans. Pattern Anal. Mach. Intell.*, vol. 13, no. 6, pp. 583–598, Jun. 1991.

[35] L. Ibanez, W. Schroeder, L. Ng, and J. Cates, *The ITK Software Guide*. New York: Kitware, 2003.

[36] National Cancer Institute. LIDC: Datasets as a public resource. (2005). [Online]. Available: http://imaging.cancer.gov/reportsandpublications/reportsandpresentations/firstdataset.

[37] J. M. Bland and D. G. Altman, "Statistical methods for assessing agreement between two methods of clinical measurement," *Lancet*, vol. 1, pp. 307–310, 1986.
[38] J. Bland and D. Altman, "Measuring agreement in method comparison studies," *Stat. Meth. Med. Res.*, vol. 8, pp. 135–160, 1999.
[39] G. Picozzi, S. Diciotti, M. Falchini, S. Foresti, F. Gallesi, E. Cavigli, L. Livi, N. Villari, and M. Mascalchi, "Operator-dependent reproducibility of size measurements of small phantoms and lung nodules examined with low dose thin-section CT," *Investig. Radiol.*, vol. 41, no. 11, pp. 831–839, Nov. 2006.
[40] D. Yankelevitz, A. Reeves, W. Kostis, B. Zhao, and C. Henschke, "Small pulmonary nodules: Volumetrically determined growth rates based on CT evaluation," *Radiology*, vol. 217, pp. 251–256, 2000.
[41] D. Wormanns, G. Kohl, E. Klotz, A. Marheine, F. Beyer, W. Heindel, and S. Diederich, "Volumetric measurements of pulmonary nodules at multirow detector CT: In vivo reproducibility," *Eur. Radiol.*, vol. 14, pp. 86–92, 2004.
[42] J. Ko, R. Marcus, E. Bomsztyk, J. Babb, C. Stefanescu, M. Kaur, D. Naidich, and H. Rusinek, "Effect of blood vessels on measurement of nodule volume in a chest phantom," *Radiology*, vol. 239, pp. 79–85, 2006.

Stefano Diciotti (S'03–M'04) was born in Florence, Italy, in 1975. He received the Laurea degree (with honors) in electronic engineering from the University of Florence, Florence, in 2001, and the Ph.D. degree in bioengineering from the University of Bologna, Bologna, Italy, in 2005.

Since 2005, he has been a Contract Professor of biomedical technologies, University of Florence. His current research interests include medical imaging, soft computing, and CAD systems.

Dr. Diciotti is a member of the IEEE Engineering in Medicine and Biology Society.

Giulia Picozzi was born in Prato, Italy, in 1973. She received the Laurea degree in medicine and the Postgraduate degree in radiology from the University of Florence, Florence, Italy, in 1999 and 2003, respectively.

Since 2006, she has been a Researcher at the Department of Clinical Phisiopathology, University of Florence, where she is involved in research programs for lung cancer screening with computed tomography (CT), and is a Radiologist with the Italung-CT Screening Group.

Massimo Falchini was born in Florence, Italy, in 1959. He received the Laurea degree in medicine and two Postgraduate degrees in gastroenterology and in radiology from the University of Florence, Florence, in 1985, 1989, and 1989, respectively.

Since 1995, he has been a Researcher at the Department of Clinical Phisiopatology, University of Florence. His current research interests include biomedical imaging and interventional radiology.

Mario Mascalchi was born in Florence, Italy, in 1959. He received the Laurea degree (with honors) in medicine from the Medical School of the University of Florence, Florence, in 1984, two Postgraduate degrees in neurology and radiology from the University of Florence, Florence, Italy, in 1988 and 1996, respectively, and the Ph.D. degree in applied physiopathology from the University of Florence, in 1992.

In 1992, he became an Assistant Professor of the Department of Radiology, University of Pisa, Pisa, Italy. In 1998, he became a Reseacher at the University of Florence, where, in 2001, he became an Associate Processor of radiology. His current research interests include computed tomography of the lung and neuromagnetic resonance. He is the author of 150 papers in refereed journals and his impact factor (IF) is 320.

Natale Villari was born in Messina, Italy, in 1940. He received the Laurea degree (with honors) in medicine from the Medical School of Messina University, Messina, in 1964. He specialized in radiology in 1966 and nuclear medicine in 1970, all from the University of Florence, Florence, Italy, and in oncology in 1975 from Modena University, Modena, Italy.

In 1970, he became an Assistant of the Department of Radiology, University of Florence. In 1976, he was a Professor of radiology with the National University of Mogadiscio, Mogadiscio, Somalia, where in 1981, he became an Associate Processor of radiology. Since 1987, he has been a Professor of general and special odontostomatologic radiology and the Director of Radiology Unit at the University of Florence, where, since 1992, he has also been a Professor of radiology, and, in 1996, the Director of the Radiology Unit at the Department of Clinical Physiophatology. His current research interests include magnetic resonance and computed tomography. He is the author of more than 200 publications and the coauthor of many books covering subjects as general radiology and new imaging techniques.

Prof. Villari is a member of the Italian Society of Medical Radiology (SIRM), and from 1996 to1998, he was the Vice President.

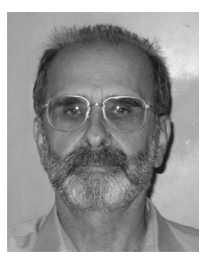

Guido Valli received the Laurea degree in physics from the University of Padua, Padua, Italy, in 1963.

Since 1982, he has been a Researcher with the National Council of Researches (CNR). In 1982, he became an Associate Professor of biomedical data and signal processing at the Faculty of Engineering, University of Florence, Florence, Italy, where since 2000, he has been a full Professor of biomedical technology. His current research interests include the study of innovative methods for the processing of biomedical data and signals, and the investigation of computer vision systems for medical diagnosis. He is the author of a number of publications and reports in the related fields.